

FUNDAMENTAL PROPERTIES AND DISTANCES OF LMC ECLIPSING BINARIES: III. EROS 1044^a

^aBASED ON OBSERVATIONS WITH THE NASA/ESA HUBBLE SPACE TELESCOPE, OBTAINED AT THE SPACE TELESCOPE SCIENCE INSTITUTE, WHICH IS OPERATED BY THE ASSOCIATION OF UNIVERSITIES FOR RESEARCH IN ASTRONOMY, INC. UNDER NASA CONTRACT NO. NAS5-26555.

IGNASI RIBAS², EDWARD L. FITZPATRICK, FRANK P. MALONEY, EDWARD F. GUINAN
Department of Astronomy & Astrophysics, Villanova University, Villanova, PA 19085

ANDRZEJ UDALSKI

Warsaw University Observatory

Submitted to the Astrophysical Journal

ABSTRACT

We present results from a detailed analysis of a third eclipsing binary (EB) system in the Large Magellanic Cloud, EROS 1044 (\sim B2 IV–V + \sim B2 III–IV). Our study combines the “classical” EB study of light and radial velocity curves with detailed modeling of the observed spectral energy distribution, and yields an essentially complete picture of the stellar properties of the system and a determination of its distance. The observational data exploited include optical photometry, space-based UV spectroscopy, and UV/optical spectrophotometry. The advantages of our technique include numerous consistency checks and, in the case of the distance determinations, the absence of zero point uncertainties and adjustable parameters. We find the EROS 1044 system to consist of a pair of normal, mildly-evolved \sim 21000 K stars, whose derived properties are consistent with stellar evolution calculations. The distance to the system is 47.5 ± 1.8 kpc. We discuss the implications of our results for three EB systems (HV 2274, HV 982, and EROS 1044) on the general distance to the Large Magellanic Cloud.

Subject headings: Binaries: Eclipsing - Stars: Distances - Stars: Fundamental Parameters - Stars: Individual (EROS 1044) - Galaxies: Magellanic Clouds - Cosmology: Distance Scale

1. INTRODUCTION

This is the third in a series of papers presenting results from detailed analyses of detached main sequence B-type eclipsing binary (EB) systems in the Large Magellanic Cloud (LMC). The main scientific goals of this program are: 1) to determine an essentially complete description of the stellar properties of each system (including temperature, mass, luminosity, and radius); and 2) to measure a precise distance for each system, from which the general distance to the LMC may be derived. The former goal allows for rigorous testing of the predictions of stellar structure and evolution theory, while the latter addresses the important role the LMC plays in the calibration of the cosmic distance scale and seeks to reduce the uncertainty in the LMC’s distance — currently 10–15% — to a level of a few percent.

Our analysis is data-intensive, requiring precise photometry (yielding light curves), high-resolution spectroscopy (yielding radial velocity curves), and UV-optical spectrophotometry spanning the range \sim 1200–7000 Å. In addition to the derivation of fundamental stellar quantities, the benefits of the analysis include numerous consistency checks and, in the case of the distance determinations, the absence of zero point uncertainties and adjustable parameters. In fact, the only parameter not explicitly determined directly is the extinction ratio R ($\equiv A(V)/E(B-V)$). (This quantity is, however, potentially measurable — although not with currently available data.) Our results do depend somewhat on stellar atmosphere models, although the main implication of this is to restrict the temperature and evolutionary state of the selected targets to a range within which the models are known to be physically appropriate and to yield precise and accurate results. This dependence on

model atmospheres leads to our focus on only detached, mildly evolved, early-B EBs.

In our previous studies, we examined the LMC EB systems HV 2274 (Guinan et al. 1998, hereafter “Paper I”; Ribas et al. 2000a) and HV 982 (Fitzpatrick et al. 2002, “Paper II”). The apparent locations of these systems in the LMC can be seen in Figure 1. For HV 2274, located in the LMC’s Bar, we find a distance of 47.0 ± 2.2 kpc (corresponding to a distance modulus of $V_0 - M_V = 18.36$ mag). HV 982, located somewhat north of the Bar and in the apparent vicinity of the 30 Doradus complex, yields a larger distance of 50.2 ± 1.2 kpc (corresponding to $V_0 - M_V = 18.50$ mag). Given the uncertainties, these results are apparently compatible but, when corrected for the most commonly assumed orientation of the LMC, they predict distances to the LMC’s optical center which differ by nearly 5 kpc. This might indicate a large line-of-sight spread in the distribution of early-type LMC stars, or perhaps a problem with the assumed LMC orientation. This issue can only be resolved by observation and analysis of other EB systems, located along a variety of sightlines.

In this paper we apply our analysis to a third LMC EB system, EROS 1044, and derive its stellar properties and distance. This system consists of two mildly evolved \sim B2 stars, with an orbital period of 2.73 days, and $V \simeq 15.2$. Preliminary determinations of distance and absolute dimensions were discussed by Maloney et al. (2000, 2001). EROS 1044 was discovered by the EROS microlensing project (Grison et al. 1995) and has also been observed by the OGLE microlensing project (Udalski, Kubiak, & Szymanski 1997), with an OGLE designation of LMC_SC7 254744. While EROS and OGLE, as well as the MACHO program (Alcock et al. 1997), are directed toward the discovery of compact objects in the halo of the Milky Way,

²Currently at Departament d’Astronomia i Meteorologia, Universitat de Barcelona, Av. Diagonal, 647, E-08028 Barcelona, Spain

these programs have produced extremely valuable photometric archives of variable stars in the LMC — notably eclipsing binaries and Cepheid variables. These resources provide extensive masterlists from which objects can be selected for further study. In the present case, EROS 1044 was originally selected from the EROS catalog based on the properties of its brightness and its light curve, indicating a detached system with deep and total eclipses.

In §2, we describe the data included in this study. In §3, the three components of the analysis (involving the light curve, radial velocity, curve and spectral energy distribution) are discussed and their individual results presented. Some aspects of our results relating to the interstellar medium towards EROS 1044 are described in §4, including an indication of the relative location of the system within the LMC. In §5, we show how the results of the analyses combine to yield a thorough description of the stellar properties of EROS 1044, and we examine the consistency of the results with stellar evolution theory. Finally, in §6, we show how the distance to the system is derived from our analysis and compare it with our previous results.

2. THE DATA

Three distinct datasets are required to carry out our analyses of the LMC EB systems: precise differential photometry (yielding light curves), high-resolution spectroscopy (yielding radial velocity curves), and multiwavelength spectrophotometry (yielding temperature and reddening information). Each of these three are described briefly below.

As in our previous papers, the primary (P) and secondary (S) components of the EROS 1044 system are defined photometrically and refer to the hotter and cooler components, respectively.

2.1. Optical Photometry

CCD differential photometric observations of EROS 1044 were obtained by both the EROS and OGLE projects. EROS data were secured with a 40-cm telescope between 1991 and 1992, and consist of 511 measurements in the blue ($\lambda \sim 4900$ Å) and 542 measurements in the red ($\lambda \sim 6700$ Å). Photometric indices were obtained via the technique of point spread function fitting. The OGLE data were acquired between 1997 and 2000 with the 1.3-m Warsaw telescope at Las Campanas Observatory, Chile, and consist of 410 I -band measurements. In this case, the technique of Difference Image Analysis was employed to derive photometric measurements, as described in Zebur, Soszynski, & Wozniak (2001).

The only available ephemeris for EROS 1044 comes from the EROS catalogue, which indicates $P = 2.727$ days. With a much longer time baseline now available, we attempted to refine the orbital period and determine a new reference epoch. We soon discovered what appears to be a discrepancy with the Julian Dates provided in the EROS light curve database. Several tests indicated a difference of about 0.125 days (= 3 hours) between the expected times and the listed EROS times. This 3-hour difference is suspicious and may result from the listing of Chilean local time (where the observations were acquired) rather than UTC (Pritchard, private communication). We therefore decided to ignore the EROS absolute time scale altogether and base the period determination solely on the time intervals within the OGLE and EROS observations. Thus, a new orbital ephemeris was determined through simultaneous minimization

of the residuals of both EROS and OGLE light curves. This approach proved to be successful (due, essentially to the long time span of the OGLE observations) and yielded the following accurate ephemeris:

$$T(\text{Min I}) = \text{HJD}2450868.2518 + \frac{2.727125}{7} E$$

The resultant light curves are well-defined, as shown in Figure 2, with the EROS observations having somewhat greater scatter than the OGLE data. The light curves exhibit primary and secondary minima with nearly equal depths of ~ 0.35 mag. The portions of the light curve between eclipses show small brightness variations presumably arising from the ellipticity of the stars and reflection effects.

The OGLE database also contains V-band measurements for EROS 1044. While the number of these (~ 35) is insufficient for our light curve analysis, they nevertheless provide a measure of the out-of-eclipse V magnitude for the EROS 1044 system, which is $V_{\text{max}} = 15.265 \pm 0.020$.

2.2. UV Spectroscopy

Radial velocity curves for EROS 1044 were derived from UV spectra obtained by us between December 2000 and January 2001 with the Space Telescope Imaging Spectrograph (STIS) of the *Hubble Space Telescope* (HST). The observations were made using the FUV-MAMA detector, with the $52'' \times 0.5''$ aperture and G140M grating. We secured nine spectra of EROS 1044 – near orbital quadratures – covering the wavelength range 1294–1348 Å, with a spectral resolution of $\lambda/\Delta\lambda \simeq 15500$, and a S/N of $\sim 20:1$. The plate scale of the data is 0.05 Å pix^{-1} (12 km s^{-1} pix^{-1}) and there are 1.7 pixels per resolution element. Identical instrumental setups were used for all observations. The exposure time per spectrum was ~ 2200 s, sufficiently short to avoid significant radial velocity shifts during the integrations. All the EROS 1044 observations were reduced using the standard HST pipeline reduction software. The dataset identifiers are O665A1010, O665A1020, O665A2010, O665A2020, O665A3010, O665A4010, O665A5010, O665A6010, and O665A7010.

For illustration, one of the HST/STIS spectra of EROS 1044 (O665A2020), taken at phase 0.79, is shown in Figure 3. For reference, a synthetic model is shown above the STIS spectrum, with prominent stellar features identified. The model was constructed by Doppler shifting and combining two synthetic spectra, each computed using R.L. Kurucz’s *ATLAS9* atmosphere models and I. Hubeny’s spectral synthesis program *SYNSPEC*. The determination of the appropriate stellar parameters² discussed in §3, and all the stellar properties are summarized in §5. The strong absorption complexes near 1302.5 Å, 1305 Å, and 1336 Å are interstellar in origin, arising in both Milky Way and LMC gas, and result from O I (λ 1302.2), Si II (λ 1304.4), and C II ($\lambda\lambda$ 1334.5, 1335.7), respectively.

Radial velocities were measured from the HST/STIS data using the “spectral disentangling” technique. As discussed in Paper II, this technique assumes that an observed double-lined spectrum is a linear combination of two single-lined spectra (one per component) at different relative velocities (determined

²The synthetic spectrum for the distorted secondary star was computed by assuming a constant mean temperature over the surface even though differences of $\sim 3\%$ between the polar and the equatorial temperatures are expected.

by the orbital phase at the time of observation). The analysis yields the two single-line spectra and the set of relative velocities for each observed spectrum by considering the entire dataset simultaneously. The practical implementation of spectral disentangling in our case was done through the Fourier disentangling code *KOREL* developed by Hadrava (1995, 1997). The spectral data were prepared for analysis with *KOREL* by rebinning to 1024 equal radial velocity bins. Data in the regions affected by interstellar absorption were masked out by setting the normalized flux between 1301.6–1305.8 Å and 1334.0–1338.3 Å to unity. A large number of *KOREL* runs from different starting points were carried out to explore the parameter space and make estimations of the uncertainties.

The radial velocities produced by the *KOREL* analysis are not heliocentric, but rather are referred to the barycenter of the binary system. Thus, the systemic velocity must be determined to correct the radial velocities to the heliocentric system. To do so, we considered the individual disentangled HST/STIS spectra and followed three different approaches; namely, gaussian fitting to well-resolved lines, cross-correlation against an observed spectrum, and cross-correlation against a synthetic spectrum. For the first approach, line identification was accomplished through comparison with the spectral atlas of Rogerson (1985). When cross-correlating with an observed spectrum, the star chosen as a template was the SMC star AzV 304 (B0.5 V) which was observed with HST/STIS in the same spectral region (dataset identifier O51901030). All three approaches yielded very similar results, with systemic radial velocities of $v_\gamma = 257.7, 263.4,$ and 260.3 km s^{-1} , respectively. The value finally adopted, $v_\gamma = 261.4 \pm 4.6 \text{ km s}^{-1}$, is the weighted average of these three with the corresponding uncertainty.

The final heliocentric radial velocities derived from all the HST/STIS spectra using the procedure outlined above are listed in Table 1, along with the date of observation and the corresponding phase. The individual errors of the velocities are not provided by *KOREL* and a reliable estimation is not straightforward. This issue is addressed in more detail in §3.2. As a reality check on our results, individual radial velocities were also measured independently using two additional procedures: gaussian fits to the strong Si III and C II features, and cross-correlation of every spectrum against the HST/STIS spectrum of AzV 304. Both methods yielded velocities compatible with those in Table 1, although with significantly larger uncertainties.

2.3. UV/Optical Spectrophotometry

We obtained spectrophotometric observations of EROS 1044 at UV and optical wavelengths with the Faint Object Spectrograph (FOS) aboard HST on 20 December 1996, at binary phase 0.138. Data were obtained in four wavelength regions, using the G130H, G190H, G270H, and G400H observing modes of the FOS with the $3.7'' \times 1.3''$ aperture, yielding a spectral resolution of $\lambda/\Delta\lambda \simeq 1300$. The dataset identifiers are Y3FU0B03T, Y3FU0B06T, Y3FU0B05T, and Y3FU0B04T, respectively. The data were processed and calibrated using the standard pipeline processing software for the FOS. As will be discussed further in §3.3, each of the FOS spectra was scaled, by a mean amount of +2.7%, to normalize them to a fiducial phase of 0.25. The four individual observations were then merged to form a single spectrum which covers the range 1145 Å to 4790 Å.

Additional HST spectrophotometric observations of EROS 1044 were carried out with STIS to extend the wavelength coverage. Data were obtained on 01 January 2001

(phase 0.30) and 25 December 2000 (phase 0.80) in the G430L and G750L observing modes, respectively, with the $52'' \times 0.5''$ aperture (yielding a spectral resolution of $\lambda/\Delta\lambda \simeq 750$). The dataset identifiers are O665A1030 and O665A2030, respectively. The data were processed and calibrated using the standard pipeline processing software. Cosmic ray blemishes were cleaned manually and the spectra were trimmed to the regions 3210–5690 Å and 5290–7490 Å for the G430L and G750L data, respectively. The two spectra were scaled, by less than +1%, to normalize them to phase 0.25. Because of concerns about photometric stability, the two STIS spectra were not merged (see §3.3).

3. THE ANALYSIS

Our study of EROS 1044 proceeds from three separate but interdependent analyses. These involve the light curve, the radial velocity curve, and the spectral energy distribution (SED). The combined results provide essentially a complete description of the physical properties of the EROS 1044 system and an accurate measurement of its distance. Each of the three analyses is described below.

3.1. The Light Curve

The fits to the light curves were carried out using an improved version of the Wilson-Devinney (W-D) program (Wilson & Devinney 1971) that includes a model atmosphere routine developed by Milone, Stagg & Kurucz (1992) for the computation of the stellar radiative parameters, based on the *ATLAS9* code. A detached configuration was chosen for all solutions. Both detailed reflection model (MREF=2, NREF=1) and proximity effect corrections were taken into account when fitting the light curves. The bolometric albedo and the gravity-brightening coefficients were both set at the canonical value of 1.0 for stars with radiative envelopes. For the limb darkening we used a logarithmic law as defined in KlingleSmith & Sobieski (1970), with first- and second-order coefficients interpolated at each iteration for the exact T_{eff} and $\log g$ of each component from a set of tables computed in advance using a grid of *ATLAS9* model atmospheres. A mass ratio of $q = M_S/M_P = 1.178$ was adopted from the spectroscopic solution (§3.2), and the temperature of the primary component was set to 21400 K, as discussed in §3.3. A circular orbit was adopted for the system as suggested by the equal width of the eclipses and the occurrence of the secondary minimum at phase 0.5. Test runs of W-D with eccentricity and argument of the periastron as free parameters yielded a value of $e = 0.0009 \pm 0.0012$ thus confirming an effectively null eccentricity (see §5 for further explanations). Finally, both components were assumed to rotate synchronously with the orbital period.

The iterations with the W-D code were carried out automatically until convergence, and a solution was defined as the set of parameters for which the differential corrections suggested by the program were smaller than the internal probable errors on three consecutive iterations. As a general rule, several runs with different starting parameters are used to make realistic estimates of the uncertainties and to test the uniqueness of the solution.

To run the solutions we focused initially on the OGLE light curve, which exhibits about half the scatter of the EROS light curves. The relative weight of the observations was set according to the photometric uncertainties of the magnitude measurements (i.e. “noise-dependent” weights). In our initial runs

we solved for the following light curve parameters: the orbital inclination (i), the temperature of the secondary ($T_{\text{eff},S}$), the gravitational potentials (Ω_P and Ω_S), the luminosity of the primary (L_P), and a phase offset ($\Delta\phi$). Convergence was achieved rapidly but, when analyzing the residuals, a significant systematic trend near the quadratures became evident. Subsequent tests revealed that the systematic deviations from the model light curve were caused by the presence of an additional source of light in the system. Thus, the fraction of “3rd light” was allowed to vary and convergence was reached for a contribution of $\sim 12.5\%$ to the total light of the system (at phase 0.25). Note that, while usually poorly determined, “3rd light” can be fairly easily constrained in this case due to the out-of-eclipse variations of the light curve caused by the mild ellipticity of the secondary component. Examination of the acquisition images for the HST/STIS observations of EROS1044 (§2.2) revealed that the source of the “3rd light” is unresolved at a level of $\sim 0''.2$.

Using the solution discussed above as starting point, we ran W-D fits to all three available light curves simultaneously and allowing for variable “3rd light” contributions. The relative weights of the light curves were set iteratively and adopted as the r.m.s. residuals of the W-D fits. These turned out to be 0.014, 0.013 and 0.006 mag for the EROS B_E , EROS R_E , and OGLE I light curves, respectively. The resulting orbital and physical parameters are well-defined and the best-fitting model light curves, together with the O–C residuals for the OGLE photometry, are shown in Figure 2.

The final orbital and stellar parameters adopted from the light curve analysis are listed in Table 2. The uncertainties given in this table were not adopted from the formal probable errors provided by the W-D code, but instead from numerical simulations and other considerations. Several sets of starting parameters were tried in order to explore the full extent of the parameter space. Special attention was paid to the error contribution from the uncertainty in the fraction of “3rd light”. In addition, the W-D iterations were not stopped after a solution was found, instead, the program was kept running to test the stability of the solution and the geometry of the χ^2 function near the minimum. The scatter in the resulting parameters from numerous additional solutions yielded estimated uncertainties that we consider to be more realistic, and are generally several times larger than the internal statistical errors.

Previous analyses of the EROS B_E and R_E light curves had been carried out by Kang et al. (1997) and Tobin et al. (1997) using W-D. These authors, however, had no radial velocity data to determine the mass ratio of the system. Kang et al. ran solutions with $q = 1$ and Tobin et al. were able to constrain the mass ratio within $q = 1 \pm 0.2$. More importantly, neither of the two analyses introduced a “3rd light” contribution in the fitting procedure. Because of this, the orbital and stellar properties presented in these works differ significantly from those of the current paper.

3.2. The Radial Velocity Curve

The radial velocity curve was fit using the same version of the W-D program as described above. The free parameters were: the orbital semi-major axis (a), the mass ratio ($q \equiv M_S/M_P$), and a velocity zero point (the systemic radial velocity v_γ). (Note that fitting a and q is equivalent to fitting the velocity semiamplitudes K_P and K_S .) The rest of the parameters were set to those resulting from the light curve solutions discussed in the previous section. The best fit to the radial velocity curve is shown in Figure 4. The fit residuals (indicated as “O–C” in

Figure 4 and in the last two columns of Table 1) correspond to r.m.s. errors of 3.1 and 3.3 km s $^{-1}$ for the primary and secondary components, respectively. These small internal errors reflect the excellent performance of the disentangling technique.

The parameters resulting from the radial velocity curve fit are listed in Table 2. The uncertainties given in the table are not taken directly from the W-D output, since they fail to account for any systematic effects that could be present in the velocity data. Instead, we estimated more realistic errors by considering the scatter of the velocities derived from the disentangling analysis of separate spectral regions. In addition, the STIS Instrument Handbook quotes a 2σ uncertainty in the absolute wavelength scale of 0.5–1.0 pix. This means, in our case, a standard error of about 4 km s $^{-1}$. By taking all these considerations into account, the uncertainties of the velocity semiamplitudes K_P and K_S were adopted as 5.1 and 5.2 km s $^{-1}$, respectively, and the errors for the rest of the radial velocity curve parameters in Table 2 were scaled accordingly.

3.3. The UV/Optical Energy Distribution

3.3.1. The Fitting Procedure

The observed SED $f_{\lambda\oplus}$ of a binary system depends on the surface fluxes of the individual components, the stellar radii, and on the attenuating effects of distance and interstellar extinction. Modeling the shape and level of the SED over a wide wavelength region can therefore yield determinations of both intrinsic and extrinsic properties of the system.

Specifically, the observed flux can be expressed as:

$$f_{\lambda\oplus} = \left(\frac{R_P}{d}\right)^2 [F_\lambda^P + (R_S/R_P)^2 F_\lambda^S] \times 10^{-0.4E(B-V)[k(\lambda-V)+R(V)]}$$

where F_λ^i $\{i = P, S\}$ are the surface fluxes of the primary and secondary stars, the R_i are the absolute radii of the components, and d is the distance to the binary. The last term carries the extinction information, including $E(B-V)$, the normalized extinction curve $k(\lambda-V) \equiv E(\lambda-V)/E(B-V)$, and the ratio of selective-to-total extinction in the V band $R(V) \equiv A(V)/E(B-V)$. We represent the stellar surface fluxes with R. L. Kurucz’s *ATLAS9* atmospheres and use a parameterized representation of UV-through-IR extinction based on the work of Fitzpatrick & Massa (1990) and Fitzpatrick (1999; hereafter F99). The Kurucz models are each functions of four parameters (T_{eff} , $\log g$, [m/H], and microturbulence velocity μ), and the extinction curves are functions of six parameters (see F99).

We model the observed SED by performing a non-linear least squares fit to determine the best-fit values of all parameters which contribute to the right side of equation 1. For EROS 1044 (as in Papers I and II), we can make several simplifications which reduce the number of free parameters in the problem: (1) the temperature ratio of the two stars is known from the light curve analysis; (2) the surface gravities can be determined by combining results from the light and radial velocity curve analyses and are $\log g = 4.04$ and 3.72 for the primary and secondary stars, respectively (see §5); (3) the values of [m/H] and μ can be assumed to be identical for both components; (4) the ratio R_S/R_P is known; and (5) the standard mean value of $R(V) = 3.1$ found for the Milky Way can reasonably be assumed given the existing LMC measurements (e.g., Koornneef 1982; Morgan & Nandy 1982; see §4).

In contrast to our previous studies, the two components of EROS 1044 have significantly different properties, with the

secondary star being about twice as bright as the primary at all observed wavelengths. As a result, its properties (particularly its radius) are better-determined than the primary’s. Since equation (1) is symmetric to the identity of the primary and secondary stars, we therefore reference our SED analysis to the secondary star. Given the simplifications noted above, we model EROS 1044’s SED by solving for the best-fitting values of T_{eff}^S , $[m/H]_{\text{PS}}$, μ_{PS} , $(R_S/d)^2$, $E(B-V)$, and six $k(\lambda-V)$ parameters — a total of 11 free parameters.

We prepared the three spectrophotometric datasets (one merged FOS spectrum and two STIS spectra) for the SED analysis by (1) velocity-shifting to bring the centroids of the stellar features to rest velocity; (2) correcting for the presence of a strong interstellar H I Ly α absorption feature in the FOS spectrum at 1215.7 Å (see §4); and (3) binning to match the *ATLAS9* wavelength grid. The statistical errors assigned to each bin were computed from the statistical errors of the original data, i.e., $\sigma_{\text{bin}}^2 = 1/\Sigma(1/\sigma_i^2)$, where the σ_i are the statistical errors of the individual spectrophotometric data points within a bin. For all the spectra, these binned uncertainties typically lie in the range 0.5% to 1.5% of the binned fluxes. The nominal weighting factor for each bin in the least squares procedure is given by $w_{\text{bin}} = 1/\sigma_{\text{bin}}^2$. We exclude a number of individual bins from the fit (i.e., set the weight to zero) for the reasons discussed by FM99 (mainly due to the presence of interstellar gas absorption features).

As discussed in Paper II, we do not merge the FOS and STIS data into a single spectrum, but rather perform the fit on the three binned spectra simultaneously and independently. We assume that the FOS fluxes represent the “true” flux level and account for zero point uncertainties in the STIS data by incorporating two zeropoint corrections (one for each STIS spectrum) in the fitting procedure. We later explicitly determine the uncertainties in the results introduced by zeropoint uncertainties in FOS.

3.3.2. Special Considerations for EROS 1044

The fact that the EROS 1044 light curve is not flat between eclipses — resulting from a mild distortion of the secondary star — complicates the SED analysis. Unless all the spectrophotometric data are obtained at the same phase, brightness offsets of up to $\sim 3\%$ may occur between spectra. To correct for this, we adjust all spectra to the phase of maximum brightness (phase = 0.25), i.e., the point at which each star displays its maximum cross-section. This correction amounts to the simple application of a multiplicative scale factor³, derived from the *B*, *R*, and *I* light curves. The offsets applied to the HST/FOS and HST/STIS data are: +3.2% for FOS/G130H, +2.3% for FOS/G190H, +2.5% for FOS/G270H, +2.7% for FOS/G400H, +0.3% for STIS/G430L, and +0.7% for STIS/750L. The offsets were applied to the FOS data prior to merging them into a single spectrum.

Because the “3rd light” source in the EROS 1044 light curve is unresolved in the HST acquisition images (see §3.1), the flux contribution is also present in the spectrophotometric data and must be accounted for in the SED analysis. The light curve data provide strong constraints on the nature of this third body. Anticipating the reddening derived below, the object’s fractional contribution at *V* ($\sim 12.5\%$) implies $V_0(\text{3rd light}) \simeq 17.3$. The constancy of the fraction of “3rd light” from the *B* through the

I bands indicates that it is an early-B star (like the EROS 1044 system). More specifically, T_{eff} must be greater than ~ 12000 K, or else the *I* band would show significantly greater contribution than *B*, and must be less than ~ 22000 K, since a hotter star — even if it were on the ZAMS — would be brighter than observed.

With these constraints in mind, we include a constant contribution in the fit to EROS 1044’s SED, produced by an *ATLAS9* model with $T_{\text{eff}} = 17000$ K and $\log g = 4.1$, appropriately scaled to produce 12.5% of the observed light in the *B*, *R*, and *I* bands at phase 0.25. The adopted T_{eff} is simply the center of the allowed range and the $\log g$ corresponds to a star of the appropriate brightness (as estimated from stellar evolution calculations). The addition of the “3rd light” to the SED analysis adds no new free parameters, but does add some uncertainty to the results. To evaluate this uncertainty, we assume 1σ ranges in T_{eff} and flux level of 14000–20000 K and 10–15%, respectively (i.e., ± 3000 K and $\pm 2.5\%$ around the nominal values). The value of $\log g$ has no influence on the results. In §5 we discuss briefly the possible nature of this star.

3.3.3. The Results

As in our previous papers, we computed the final fit to EROS 1044’s SED after adjusting the weights in the fitting procedure to yield a final value of $\chi^2 = 1$ — since the statistical errors of the data under-represent the total uncertainties (see the discussion in Paper II). This was accomplished by quadratically adding an uncertainty equivalent to 1.75% of the local binned flux to the statistical uncertainty of each flux point. (Essentially identical results occur if the statistical errors are simply scaled by a factor of 2.2 to yield $\chi^2 = 1$.) This value of 1.75% gives an indication of the general quality of the fit to EROS 1044’s SED, excluding the effect of statistical noise. It is comparable the quality level we have seen in the previous analyses (1.5% for HV 2274; 2.0% for HV 982).

The best-fitting values of the energy distribution parameters for EROS 1044 and their $1-\sigma$ uncertainties (“internal errors”) are listed in Tables 2 (stellar properties), 3 (STIS offsets), and 4 (extinction curve parameters). The internal errors were evaluated by quadratically combining (for each parameter) the uncertainties from the fitting procedure (computed using the full correlations) with the errors induced by variations of the T_{eff} and flux level of the “3rd light” within the $1-\sigma$ ranges specified above. A comparison between the observed spectra and the best-fitting model is shown in Figure 5. The three binned spectra are plotted separately in the figure for clarity (small filled circles). The zeropoint offset corrections (see Table 3) were applied to all STIS spectra in Figure 5. Note that we show the quantity $\lambda f_{\lambda\oplus}$ as the ordinate in Figure 5 (rather than $f_{\lambda\oplus}$) strictly for display purposes, to “flatten out” the energy distributions.

The correction factors of 6.7% and 4.5% required to rectify the STIS G430L and G750L spectra, respectively, are similar to the results found for HV 982 in Paper II. This apparently systematic effect probably results from light-loss in the STIS 0’’5 slit. This will be tested by using a wider slit in future STIS observations.

4. THE INTERSTELLAR MEDIUM TOWARDS EROS 1044

³The application of a multiplicative scale factor is granted by the small variations in the relative light ratio (primary, secondary, and “3rd light”) between the phases of the FOS observations and phase 0.25. The relative contribution of the “3rd light” varies by only 0.3% and changes in the light ratio between the primary and the secondary amount to a mere 0.1% effect.

We measure the column density of interstellar H I in the foregrounds of the stars in our program by comparing their observed H I Ly α 1216.7 Å absorption line profiles with theoretical profiles consisting of a synthetic stellar spectrum convolved with an interstellar absorption profile. The interstellar profile is constructed assuming a component at 0 km s⁻¹ with $N(\text{H I}) = 5.5 \times 10^{20}$ cm⁻², corresponding to Milky Way foreground gas (see, e.g., Schwering & Israel 1991), and a second component with a LMC-like velocity and a column density which is varied to produce the best fit to the data (as judged by visual inspection).

The best-fitting Ly α profile for EROS 1044 can be seen in Figure 6, where we illustrate the unbinned FOS spectrum, the synthetic stellar spectrum (dotted line) and the convolution of the synthetic spectrum with the interstellar profile (thick solid curve). The LMC component of the interstellar profile is located at $v = 257$ km s⁻¹ (from the H I 21 cm results of Rohlfs et al. 1984) with a best-fitting column density of 2.0×10^{20} cm⁻². The relatively noisy FOS spectrum, strong Ly α geocoronal contamination (which fills in the bottom of the line), and the strength of the stellar feature conspire to make this measurement somewhat uncertain. We estimate a $\sim 2\sigma$ range of $\sim \pm 2 \times 10^{20}$ cm⁻², i.e., it is barely possible that EROS 1044 is “above” all the LMC H I in its direction (although this is not consistent with the presence of LMC reddening, as discussed below), and unlikely that it is behind more than $\sim 4 \times 10^{20}$ cm⁻² of LMC H I.

The value of $E(B-V)$ found for EROS 1044 in §3, combined with a Galactic foreground reddening of $E(B-V)_{\text{MW}} = 0.055$ (from the data of Oestreich, Goehmann, & Schmidt-Kaler 1995), indicates a LMC reddening corresponding to $E(B-V)_{\text{LMC}} = 0.011$. The implied LMC gas-to-dust ratio of 1.8×10^{22} cm⁻² mag⁻¹ — with a large uncertainty — is compatible with other measurements (see Fitzpatrick 1985).

The H I 21-cm emission line survey of Rohlfs et al. (1984) reveals that the total LMC H I column density along the EROS 1044 line of sight is about 1.5×10^{21} cm⁻², centered at 257 km s⁻¹ (as noted above). This result, plus the Ly α absorption and $E(B-V)_{\text{LMC}}$ determinations, indicates that EROS 1044 is embedded within (as opposed to being behind or in front of) the main H I mass along its line of sight. In addition, the systemic velocity for EROS 1044, 261 km s⁻¹, is nearly identical to that of the H I gas. Thus, like HV2274 (which is also located in the LMC’s Bar) — and unlike HV 982 — it is clear that EROS 1044 is physically associated with the LMC’s gas and dust disk.

The interstellar extinction curve determined for the EROS 1044 sightline is shown in Figure 7. Small symbols indicate the normalized ratio of model fluxes to observed fluxes, while the thick solid line shows the parameterized representation of the extinction, which was actually determined by the fitting process. The parameters defining the curve are listed in Table 4. The $E(B-V)$ results above indicate that this curve is dominated by Milky Way foreground dust, but contains a $\sim 20\%$ contribution from LMC dust. The curve is nearly identical to the result for HV 982 in Paper II, which is also dominated by Milky Way foreground dust, and notable for the very weak 2175 Å bump. We have been granted FUSE observations for EROS 1044 that will allow us to extend the analysis into the far-UV. We will discuss the interstellar extinction results for our whole sample of LMC EBs in a future paper.

5. THE PHYSICAL PROPERTIES OF THE EROS 1044 STARS

The results of the analyses described above can be combined to provide a detailed characterization of the physical properties of the EROS 1044 system. We summarize these properties in Table 5 and indicate in the Notes to the Table how the individual stellar properties were derived.

It is important to note that the results presented so far have been obtained independently of theoretical evolution considerations. Thus, stellar evolution models can be used to provide a valuable check on the self-consistency of our empirical results. To make this comparison, we utilize the evolutionary models of Claret (1995, 1997) and Claret & Giménez (1995, 1998), together referred to as the CG models. These models cover a wide range in both metallicity (Z) and initial helium abundance (Y), incorporate the most modern input physics, and adopt a convective overshooting parameter of $0.2 H_p$.

The locations of the EROS 1044 components in the $\log T_{\text{eff}}$ vs. $\log L$ diagram are shown in Figure 8. The skewed rectangular boxes indicate the 1σ error locus (recall that errors in T_{eff} and L are correlated). The best-fitting pair of evolution tracks are also shown on the plot. These tracks correspond to the masses derived from the analysis (see Table 5). Approximate error bars for the evolution tracks, which reflect the 1σ uncertainties on the observed masses, are shown near the ZAMS. Only the helium (Y) and metal abundances (Z) were adjusted to optimize the fit. Best-fitting values were obtained through the procedure described by Ribas et al. (2000b) and standard errors are estimated through a Monte Carlo simulation. The procedure yielded values of $Y = 0.26 \pm 0.03$ and $Z = 0.007 \pm 0.003$ (i.e. $[\text{m}/\text{H}] = -0.40^{+0.16}_{-0.24}$).

The results in Figure 8 demonstrate excellent agreement between our derivation of the EROS 1044 stellar properties and expectations from stellar evolution. The stars’ positions in the $\log T_{\text{eff}}$ vs. $\log L$ diagram are consistent with their measured masses; the metallicity derived from the evolution tracks agrees with that obtained from the spectrophotometric analysis (see §3.3); and the helium abundance agrees with expectations from empirical chemical enrichment laws (see Ribas et al. 2000b). Further, the stars are consistent with a single isochrone, indicating an age for the system of 29 ± 4 Myr (dotted line in Fig. 8). We conclude that the EROS 1044 EB system consists of a pair of normal early-B stars, whose properties are well-modeled by current stellar atmosphere and structure theory.

There are compelling observational evidences indicating that the orbit of EROS 1044 is circular (see §3.1). From the data described above this can be further checked by performing theoretical tidal evolution calculations. Using the method described in Claret, Giménez, & Cunha (1995) we find that the system components synchronized their rotational velocities very soon (~ 1 Myr) after the ZAMS. Additionally, our calculations indicate that the orbit became circular at an age of 17 Myr (compared with the current 29 Myr) thus confirming the observational evidences.

Numerous EB systems have been found to be part of hierarchical triple systems, with companions in more distant orbits. Thus, it is reasonable to suspect that the “3rd light” contributing to the EROS 1044 light curve might arise from a coeval companion physically associated with the EB system. Based on the 29 Myr isochrone and on the observed brightness of the “3rd light” component, the properties of such a companion would be: $M = 5.7 M_{\odot}$, $T_{\text{eff}} = 19400$ K, $\log L/L_{\odot} = 3.09$, and $\log g = 4.20$. The position of this star on the $\log T_{\text{eff}}$ vs. $\log L$ diagram is indicated in Figure 8 by the plus sign. The temperature of the putative coeval companion is within the observationally-

allowable range (see §3.3), and thus it is plausible — although not proven — that EROS 1044 is part of a triple system. Further insight into the nature of the 3rd body might be derived from the analysis of spectrophotometry carried out during the total occultation at 0.0 phase, when the light contribution of one of the eclipsing components is not present. Also, additional determinations of eclipse times in the future could reveal the presence (and yield the mass) of the third body through the analysis the light travel time effect arising from the movement of the eclipsing pair around the barycenter of the triple system.

6. THE DISTANCE TO EROS 1044 AND THE LMC

The discussion above in §5 demonstrates that the properties of the EROS 1044 EB system are very well-characterized, are consistent with a variety of internal and external reality checks, and reveal the system to consist of a pair of normal, mildly evolved early B-type stars. For such a system, the determination of the distance is straightforward: we combine the absolute radius of the secondary star R_S (derived from the classical EB analysis) with the distance attenuation factor $(R_S/d)^2$ (derived from the SED analysis) and find $d_{\text{EROS 1044}} = 47.5 \pm 1.8$ kpc, corresponding to a distance modulus of $(V_0 - M_V)_{\text{EROS 1044}} = 18.38 \pm 0.08$.

The uncertainty in the EROS 1044 distance is estimated from considering three sources of error: (1) the internal measurement errors in R_S and $(R_S/d)^2$ given in Table 2; (2) uncertainty in the appropriate value of the extinction parameter $R(V)$; and (3) uncertainty in the FOS flux scale zeropoint due to calibration errors and instrument stability. Straightforward propagation of errors shows that these three factors yield individual uncertainties of ± 1.60 kpc, ± 0.40 kpc (assuming $\sigma R(V) = \pm 0.3$), and ± 0.60 kpc (assuming $\sigma f(\text{FOS}) = \pm 2.5\%$), respectively. The overall 1σ uncertainty quoted above is the quadratic sum of these three errors, which are considered to be independent. Recall that the internal errors for $(R_S/d)^2$ listed in Table 2 already include a conservative estimate of the uncertainty introduced by the presence of “3rd light” in the system. The only “adjustable” factor in the analysis is the extinction parameter $R(V)$, for which we have assumed the value 3.1. The weak dependence of our result on this parameter is given by: $(V_0 - M_V)_{\text{EROS 1044}} = 18.38 - 0.055 \times [R(V) - 3.1]$.

In Table 6 we summarize the distances derived for the three LMC EB systems we have analyzed so far. While the distances to the three EB’s are all mutually consistent — at a level better than $\sim 1.5\sigma$ — the results certainly do suggest that HV 982 is the most distant system, perhaps by as much as several kpc. This inference is consistent with the analyses of interstellar H I towards the stars: EROS 1044 and HV 2274 have been found to be embedded within the H I disk along their lines of sight, while HV 982 is located at an undetermined distance behind the H I disk (i.e., its H I emission and absorption column densities are identical).

Since the LMC is not observed face-on in the sky, determining its distance from those of the individual EB systems requires first choosing a reference point within the LMC and then correcting the individual results for the spatial orientation of the LMC. We take the optical center of the LMC’s Bar as our reference point, located at $(\alpha, \delta)_{1950} = (5^h 24^m, -69^\circ 47')$ according to Isserstedt (1975) and assume a disk-like configuration. For the orientation, we examine two cases. First, we assume an inclination angle of 38° and a line-of-nodes position angle of 168° (Schmidt-Kaler & Gochermann 1992). (The reference point and this orientation of the line-of-nodes are in-

dicated in Figure 1 by the open box and solid line, respectively. The “near-side” of the LMC is eastward of the line-of-nodes.) The distances implied for the LMC reference point based on this assumption are given in column 4 of Table 6 (“Case I”). The second orientation we examine is a recent result from van der Marel & Cioni (2001), who found an inclination of 34.7° and a line-of-nodes position angle of 122.5° . This orientation has the line of nodes lying nearly along the LMC’s Bar. Results based on this assumption are in column 5 of Table 6 (“Case II”).

Table 6 shows that an LMC distance based on HV 2274 is sensitive to the assumed LMC orientation, while results based on EROS 1044 and HV 982 are largely independent of the assumptions, due to their apparent proximity to the reference point. It appears that Case II best preserves the relative agreement among the distances although, given the size of the uncertainties for EROS 1044 and HV 2274, this is not yet a rigorous test of the possible LMC orientations.

We conclude that our results are thus far compatible with a single distance of ~ 48 kpc, corresponding to a distance modulus of ~ 18.4 mag. However, the result for HV 982 provides a tantalizing hint that there may be some spatial extension of the LMC along its sightline, which passes near to that of SN 1987A (see Fig. 1). Panagia (1999) finds a distance of 51.4 ± 1.2 kpc for SN 1987A, consistent with our value for HV 982. Only further observations will reveal whether the apparently well-determined HV 982 and SN 1987A distances are representative of the LMC as a whole or only of a distinct region (the 30 Doradus complex?), located behind the main mass of the LMC. The shorter distances for EROS 1044 and HV 2274 suggest this as a possible scenario although, as with the discussion of the LMC orientation above, their large uncertainties preclude firm conclusions. The precision of the EROS 1044 result is limited by the uncertain contribution of the “3rd light” component, and is unlikely to be improved. The HV 2274 result, however, is limited only by the absence of spectrophotometric data in the optical spectral region (see Paper II). The acquisition of such data could result in an improvement of HV 2274’s distance measurement to a precision comparable to that for HV 982. While conclusions drawn from HV 2274 will always be subject to assumptions on the LMC’s orientation, nevertheless, its distance does provide an upper limit to the distance of the LMC reference point, and could yield a critical counterpoint to HV 982 and SN1987A.

In general, our EB analysis is ideally suited to addressing the issues of the LMC’s spatial orientation and internal structure, since it yields precise results for individual objects which are widely distributed across the face of the LMC. We are currently analyzing data for three more systems, HV 5936, EROS 1066, and MACHO 053648.7-691700 (see Fig. 1). The apparent locations of EROS 1066 and MACHO 053648.7-691700 in the Bar and the 30 Doradus region, respectively, make them ideal for further testing the possibility that stars in the apparent vicinity of 30 Doradus may lie significantly behind the Bar. Within the next few years we hope to expand the program to include about 20 systems. Recent n -body simulations of the tidal interaction of the Milky Way with the LMC indicate that its structure may be more extended and complex than presently assumed (see Weinberg 2000). Our ensemble of targets should be able both to nail down the distance to the LMC and to provide a detailed probe of its structure and orientation.

We thank Villanova undergraduate students J. F. Sepinsky and J. E. Castora for help with data preparation and analysis.

These students were supported by the Undergraduate Summer Research Assistance Grant from the Delaware Space Grant College Consortium. Our HST Program Coordinator, Alison Vick, is warmly thanked for their invaluable help with the preparation of the observations. E. L. F. acknowledges support from NASA ADP grant NAG5-7117 to Villanova University and thanks

Michael Oestreicher for kindly making his LMC foreground extinction data available. I. R. acknowledges the Catalan Regional Government (CIRIT) for financial support through a postdoctoral Fulbright fellowship. This work was supported by NASA grants NAG5-7113, HST GO-06683, HST GO-08691, and NSF/RUI AST-9315365.

REFERENCES

- Alcock, C., et al. 1997, *ApJ*, 486, 697
 Claret, A. 1995, *A&AS*, 109, 441
 Claret, A. 1997, *A&AS*, 125, 439
 Claret, A., & Giménez, A. 1995, *A&AS*, 114, 549
 Claret, A., & Giménez, A. 1998, *A&AS*, 133, 12
 Claret, A., Giménez, A., & Cunha, N. C. S. 1995, *A&A*, 299, 724
 Fitzpatrick, E. L. 1985, *ApJ*, 299, 219
 Fitzpatrick, E. L. 1986, *AJ*, 92, 1068
 Fitzpatrick, E. L. 1999, *PASP*, 111, 63 (F99)
 Fitzpatrick, E. L., & Massa, D. 1990, *ApJS*, 72, 163
 Fitzpatrick, E. L., Ribas, I., Guinan, E. F., DeWarf, L. E., Maloney, F. P., & Massa, D. 2002, *ApJ*, 564, 260 (Paper II)
 Grison, P., et al. 1995, *A&AS*, 109, 447
 Guinan, E. F., Fitzpatrick, E. L., DeWarf, L. E., Maloney, F. P., Maurone, P. A., Ribas, I., Pritchard, J. D., Bradstreet, D. H., & Giménez, A. 1998a, *ApJ*, 509, L21 (Paper I)
 Hadrava, P. 1995, *A&AS*, 114, 393
 Hadrava, P. 1997, *A&AS*, 122, 581
 Isserstedt, J. 1975, *A&A*, 41, 21
 Kang, Y. W., DeWarf, E. F., Guinan, E. F., & Maurone, P. A. 1997, in *Variable Stars and the Astrophysical Returns of the Microlensing Surveys*, eds. R. Ferlet, J.-P. Maillard, & B. Raban (Cedex, France: Editions Frontieres), 423
 KlingleSmith, D. A. & Sobieski, S. 1970, *AJ*, 75, 175
 Koornneef, J. 1982, *A&A*, 107, 247
 Maloney, F. P., Fitzpatrick, E. L., Guinan, E. F., Kang, Y. W., Ribas, I., DeWarf, L. E., Bradstreet, D. H., & Sepinsky, J. F. 2000, *BAAS*, 31, 1483
 Maloney, F. P., Ribas, I., Fitzpatrick, E. L., Guinan, E. F., DeWarf, L. E., Castora, J. E., & Sepinsky, J. F. 2001, *BAAS*, 33, 787
 Milone, E. F., Stagg, C. R., & Kurucz, R. L. 1992, *ApJS*, 79, 123
 Morgan, D. H., & Nandy, K. 1982, *MNRAS*, 199, 979
 Oestreicher, M. O., Goehermann, J., & Schmidt-Kaler, T. 1995, *A&AS*, 112, 495
 Panagia, N. 1999, in *IAU Symp. 190, New Views of the Magellanic Clouds*, eds. Y.-H. Chu, N. Suntzeff, J. Hesser, & D. Bohlender, 549
 Ribas, I., Guinan, E. F., Fitzpatrick, E. L., DeWarf, L. E., Maloney, F. P., Maurone, P. A., Bradstreet, D. H., Giménez, A., & Pritchard, J. D. 2000a, *ApJ*, 528, 692
 Ribas, I., Jordi, C., Torra, J., & Giménez, A. 2000b, *MNRAS*, 313, 99
 Rogerson, J. B. Jr. 1985, *ApJS*, 57, 751
 Rohlfs, K., Kreitschmann, J., Siegmán, B. C., & Feitzinger, J. V. 1984, *A&A*, 137, 343
 Schmidt-Kaler, T. & Goehermann, J. 1992, in *Variable Stars and Galaxies*, ASP Conf. Ser. 30, ed. B. Warner (San Francisco: ASP), 203
 Schwing, P. B. W., & Israel, F. P. 1991, *A&A*, 246, 231
 Tobin, W., Pritchard, J. D., Zambri, M., Keep, L.-B., & Skuljan, L. 1997, in *Variable Stars and the Astrophysical Returns of the Microlensing Surveys*, eds. R. Ferlet, J.-P. Maillard, & B. Raban (Cedex, France: Editions Frontieres), 303
 Udalski, A., Kubiak, M., & Szymanski, M. 1997, *AcA*, 47, 319
 van der Marel, R. P. & Cioni, M.-R. L. 2001, *AJ*, 122, 1807
 Weinberg, M. D. 2000, *ApJ*, 532, 922
 Wilson, R. E., & Deviney, E. J. 1971, *ApJ*, 166, 605
 Zebun, K., Soszynski, I., & Wozniak, P. R. 2001, *AcA*, 51, 303

TABLE 1
 HELIOCENTRIC RADIAL VELOCITY MEASUREMENTS FOR EROS 1044

HJD (−2400000)	Orbital Phase	RV _p (km s ^{−1})	RV _s (km s ^{−1})	(O−C) _p (km s ^{−1})	(O−C) _s (km s ^{−1})
51899.9747	0.3189	78.8	421.7	1.3	1.7
51900.9220	0.6663	438.5	111.1	−2.2	0.8
51903.9330	0.7703	466.1	94.4	0.8	2.9
51903.9895	0.7911	455.6	92.1	−4.3	−4.8
51906.6639	0.7717	464.3	98.0	−0.7	6.2
51910.6085	0.2182	54.0	430.3	−7.3	−1.5
51910.6754	0.2427	56.6	435.2	−1.1	0.2
51910.7601	0.2737	58.6	433.5	−1.6	0.1
51910.8105	0.2922	68.3	435.1	2.9	5.6

TABLE 2
RESULTS FROM LIGHT CURVE, RADIAL VELOCITY CURVE, AND SPECTROPHOTOMETRY ANALYSES OF EROS 1044

Parameter	Value
<i>Light Curve Analysis</i>	
Period	2.727125 ± 0.000004 days
Eccentricity	0.0 (fixed)
Inclination	87.2 ± 0.9 deg
$T_{\text{eff}}^{\text{S}}/T_{\text{eff}}^{\text{P}}$	0.958 ± 0.008
[3rd light] _{OGLE I} ^a	$12.6 \pm 2.5\%$
[3rd light] _{EROS B} ^a	$12.7 \pm 2.5\%$
[3rd light] _{EROS R} ^a	$12.4 \pm 2.5\%$
$[L_{\text{S}}/L_{\text{P}}]_{\text{OGLE I}}$	2.37 ± 0.03
$[L_{\text{S}}/L_{\text{P}}]_{\text{EROS B}}$	2.33 ± 0.07
$[L_{\text{S}}/L_{\text{P}}]_{\text{EROS R}}$	2.35 ± 0.06
r_{P}^{b}	0.205 ± 0.005
r_{S}^{b}	0.323 ± 0.003
$r_{\text{S}}/r_{\text{P}}^{\text{c}}$	1.575 ± 0.041
$\Omega_{\text{P}}^{\text{d}}$	6.09 ± 0.11
$\Omega_{\text{S}}^{\text{d}}$	4.64 ± 0.03
<i>Radial Velocity Curve Analysis</i>	
K_{P}	205.2 ± 5.1 km s ⁻¹
K_{S}	174.2 ± 5.2 km s ⁻¹
q^{e}	1.178 ± 0.046
v_{γ}	261.4 ± 4.6 km s ⁻¹
a	20.49 ± 0.45 R _☉
<i>Energy Distribution Analysis</i>	
$T_{\text{eff}}^{\text{S}}$	20500 ± 470 K
$[\text{m}/\text{H}]_{\text{PS}}$	-0.34 ± 0.06
μ_{PS}	0 km s ⁻¹
$E(B-V)$	0.066 ± 0.004 mag
$\log(R_{\text{S}}/d)^2$	-23.007 ± 0.023

^aContribution of “3rd light” component to total observed flux, normalized at phase 0.25.

^bFractional stellar radius $r \equiv R/a$, where R is the stellar “volume radius” and a is the orbital semi-major axis.

^cValue and uncertainty computed directly from r_{P} and r_{S} . A Monte Carlo simulation was run because of concerns with possible error correlations and yielded a very similar value of $\langle r_{\text{S}}/r_{\text{P}} \rangle = 1.566 \pm 0.036$.

^dNormalized potential at stellar surface.

^eMass ratio $M_{\text{S}}/M_{\text{P}}$

TABLE 3
OFFSETS APPLIED TO HST/STIS OBSERVATIONS OF EROS 1044

HST Dataset Name	STIS Grating	Offset (FOS – STIS)
O665A1030	G430L	$+6.7 \pm 0.3\%$
O665A2030	G750L	$+4.5 \pm 0.7\%$

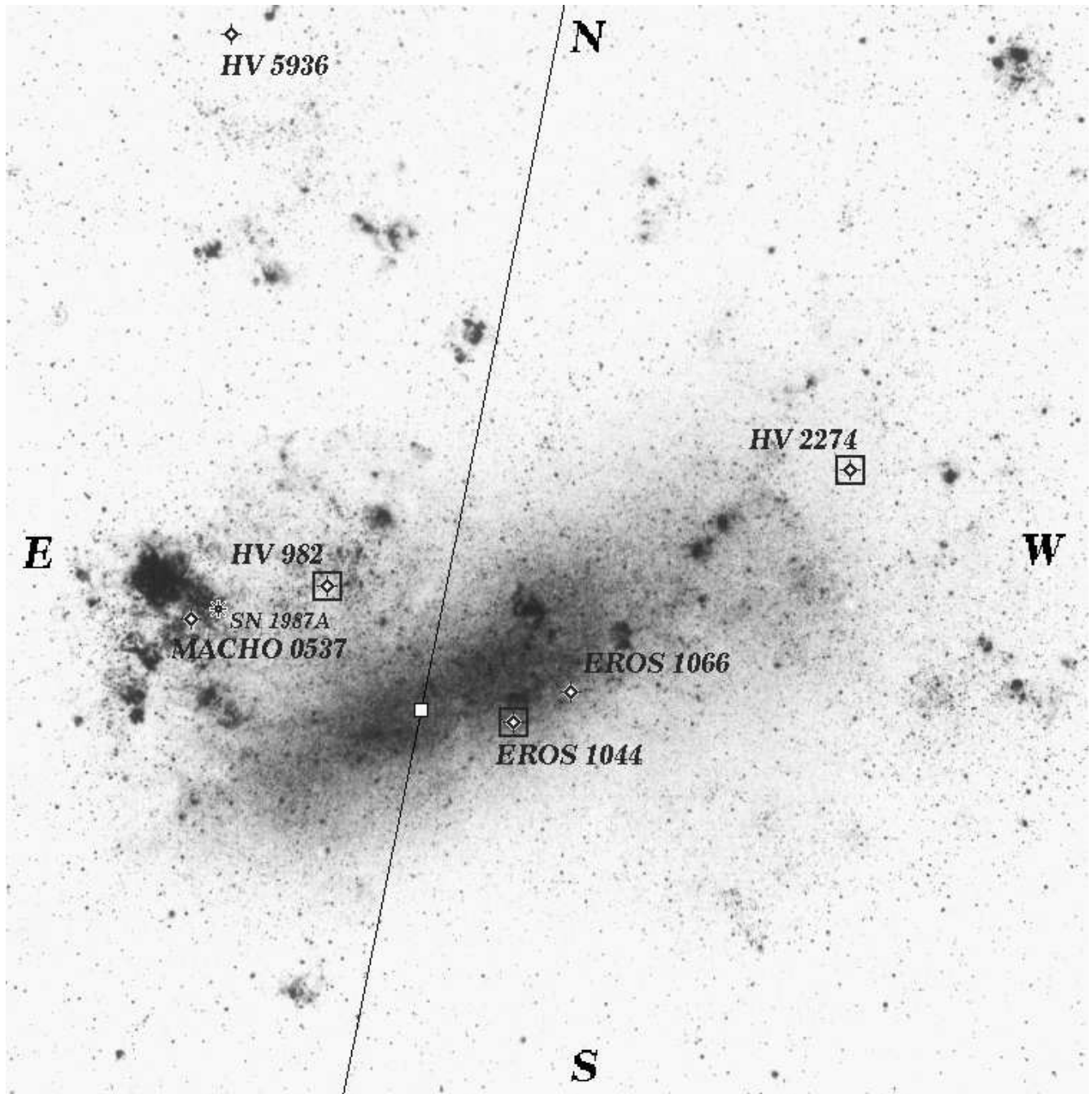


FIG. 1.— A photo of the Large Magellanic Cloud indicating the locations of EROS 1044 (this paper), HV 2274 (Paper I), HV 982 (Paper II) and three targets of future analyses, HV 5936, EROS 1066, and MACHO 053648.7-691700 (labeled in the figure as MACHO 0537). The optical center of the LMC's Bar according to Isserstedt 1975 is indicated by the open box and the LMC's line of nodes, according to Schmidt-Kaler & Goehrmann 1992, is shown by the solid line. The "nearside" of the LMC is to the east of the line of nodes. The location of SN 1987A is also indicated. Photo reproduced by permission of the Carnegie Institution of Washington.

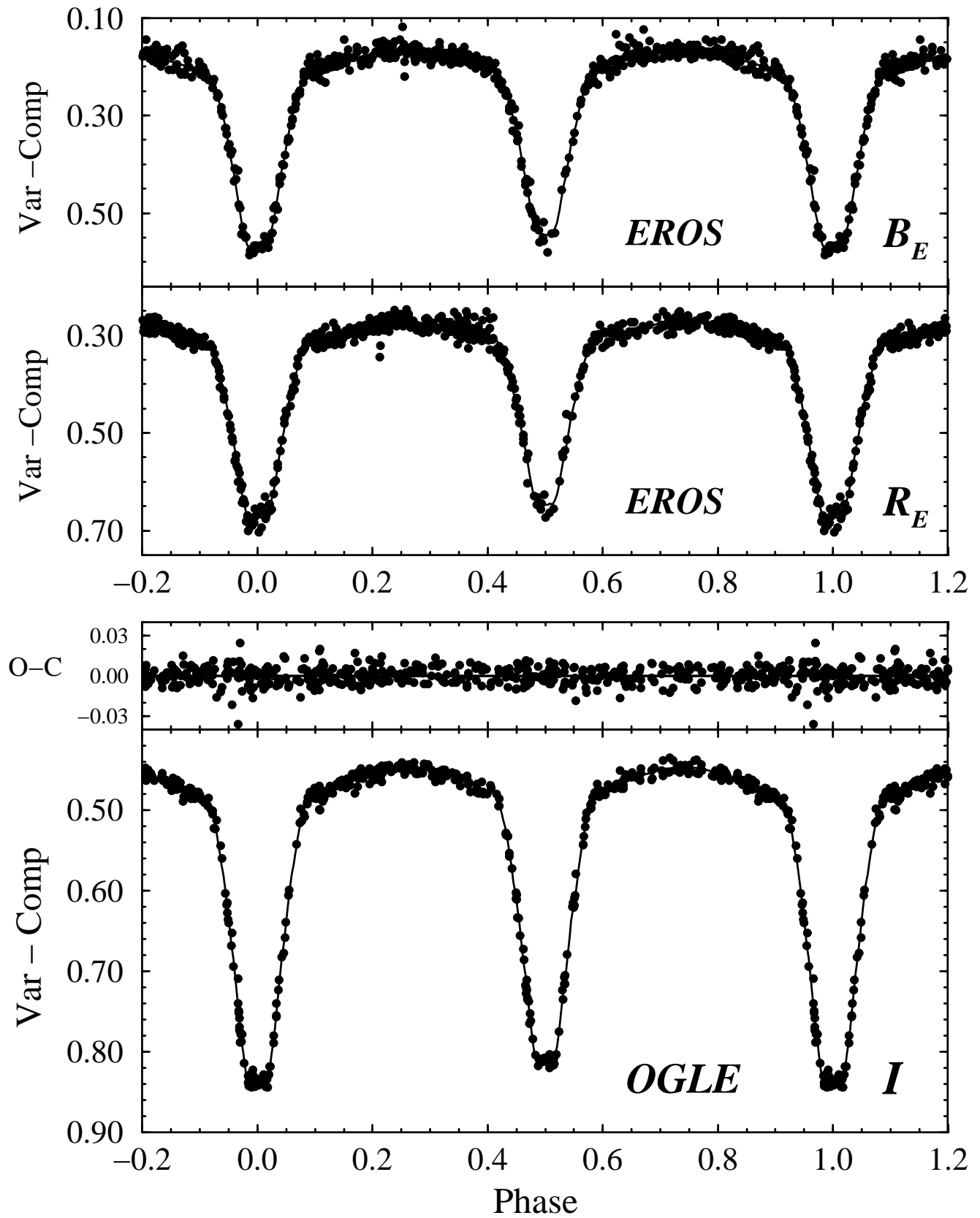


FIG. 2.— EROS B_E , EROS R_E , and OGLE I light curves for EROS 1044 (filled circles) overplotted with the best fitting model (solid curves). The residuals to the fit of the OGLE light curve (“O-C”) are shown above. The parameters derived from the fit are listed in Table 2.

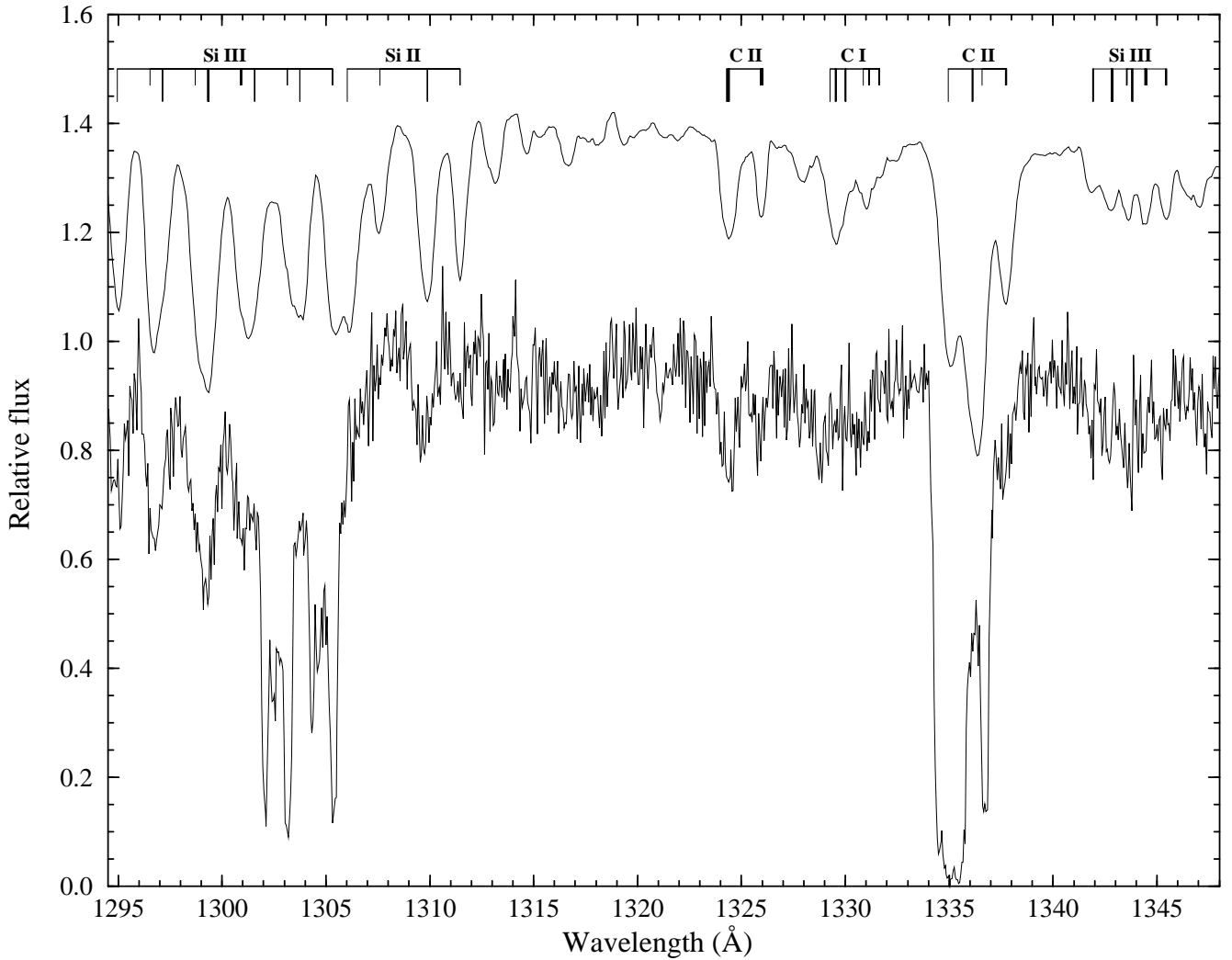


FIG. 3.— Observed spectrum of EROS 1044 obtained with HST/STIS at binary phase 0.7911. The velocities of the primary and secondary components at this phase are 459.9 km s^{-1} and 96.9 km s^{-1} , respectively. A double-line synthetic model is shown for comparison, with prominent stellar lines labeled (see §2.2). The features of the more luminous secondary star are indicated by the long tick marks, and those of the primary star by the short tick marks. The strong absorption complexes near 1302.5 Å, 1305 Å, and 1336 Å are interstellar in origin, arising in both Milky Way and LMC gas, and result from O I (λ 1302.2), Si II (λ 1304.4), and C II ($\lambda\lambda$ 1334.5, 1335.7), respectively.

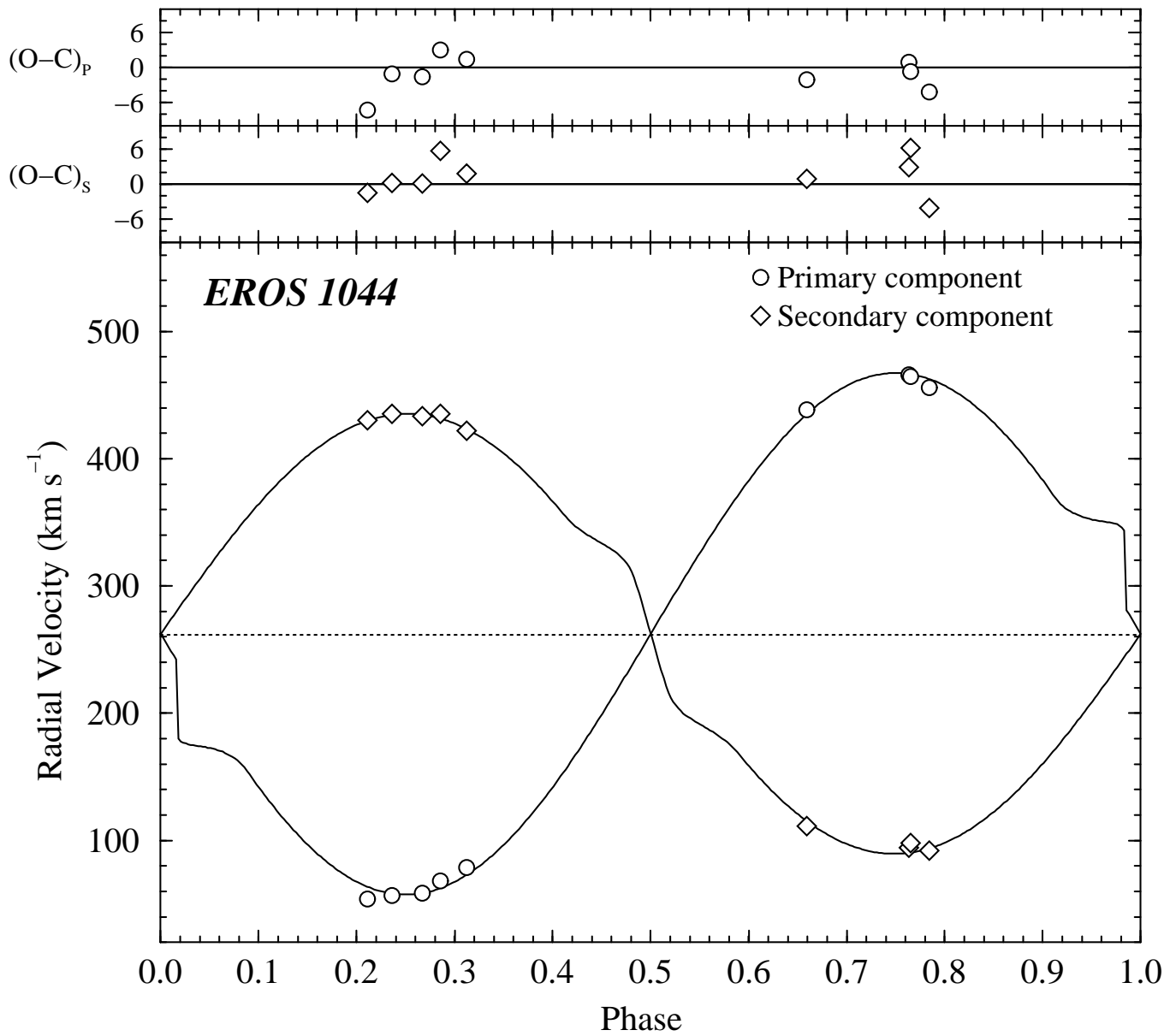


FIG. 4.— Radial velocity data for EROS 1044 (see Table 1) superimposed with best-fitting model. The parameters derived from the data are listed in Table 2. The fit assumed a circular orbit. The residuals to the fit are shown above the radial velocity curve and indicate r.m.s. uncertainties in the data of ~ 3.4 and $\sim 3.1 \text{ km s}^{-1}$ for the primary and secondary components, respectively.

TABLE 4
EXTINCTION CURVE PARAMETERS FOR EROS 1044

Parameter	Description	Value
x_0	UV bump centroid	$4.68 \pm 0.04 \mu\text{m}^{-1}$
γ	UV bump FWHM	$0.79 \pm 0.14 \mu\text{m}^{-1}$
c_1	linear offset	-0.35 ± 0.29
c_2	linear slope	0.89 ± 0.08
c_3	UV bump strength	0.69 ± 0.26
c_4	FUV curvature	0.46 ± 0.09
$R(V)$	$A(V)/E(B-V)$	3.1 (assumed)

NOTE.—The extinction curve parameterization scheme is based on the work of Fitzpatrick & Massa 1990 and the complete UV-through-IR curve is constructed following the recipe of Fitzpatrick 1999.

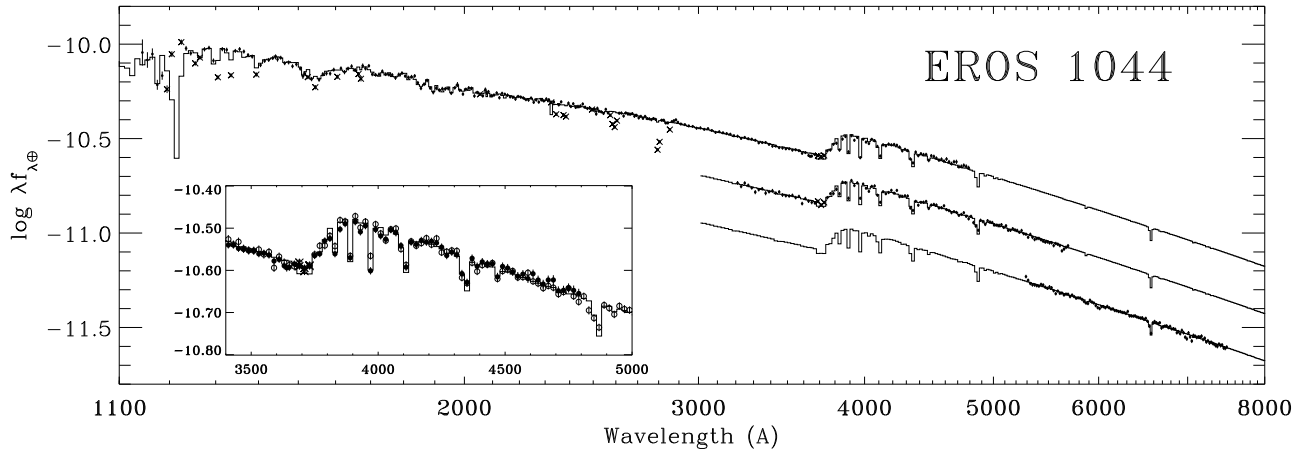


FIG. 5.— The observed UV/optical energy distribution of the EROS 1044 system (small filled circles) superimposed with the best-fitting model. The top spectrum shows the FOS data, the middle spectrum (shifted by -0.25 dex) the STIS/G430L data, and the lower spectrum (shifted by -0.5 dex) the STIS/G750L data. Vertical lines through the data points indicate the 1σ observational errors. The energy distribution fitting procedure was performed simultaneously on all three datasets. Crosses denote data points excluded from the fit, primarily due to contamination by interstellar absorption lines. The various constraints imposed on the fit are discussed in §3.3. The model, shifted to match the spectra, consists of a trio of reddened and distance-attenuated Kurucz *ATLAS9* atmosphere models (histogram-style lines), corresponding to the primary and secondary components of the binary system and the “3rd light” component. The parameters derived from the fit to the energy distribution are listed in Tables 2, 3, and 4. The inset shows a blowup of the region surrounding the Balmer Jump which illustrates the overlap between the FOS (solid circles) and STIS/G430L (open circles) data.

TABLE 5
PHYSICAL PROPERTIES OF THE EROS 1044 SYSTEM

Property	Primary Star	Secondary Star
Spectral Type ^a	B2 IV–V	B2 III–IV
V^b (mag)	16.68	15.77
Mass ^c (M_{\odot})	7.1 ± 0.5	8.4 ± 0.5
Radius ^d (R_{\odot})	4.20 ± 0.13	6.61 ± 0.14
$\log g^e$ (cgs)	4.043 ± 0.040	3.721 ± 0.030
T_{eff}^f (K)	21400 ± 525	20500 ± 470
$\log(L/L_{\odot})^g$	3.53 ± 0.05	3.85 ± 0.04
[m/H] ^h	-0.34 ± 0.06	-0.34 ± 0.06
$v \sin i^i$ (km s^{-1})	78	123
M_{bol}^j (mag)	-4.07 ± 0.13	-4.87 ± 0.10
M_V^k (mag)	-1.90	-2.82
Age ^l (Myr)		29 ± 4
$d_{\text{EROS 1044}}^m$ (kpc)		47.5 ± 1.8

^aEstimated from T_{eff} and $\log g$

^bFrom synthetic photometry of best-fitting *ATLAS9* model to the EROS 1044 system. The “3rd light” component has a (synthetic) V magnitude of 17.53. Combining these magnitudes yields $V_{\text{EROS 1044}} = 15.24$, consistent with the observational result from OGLE quoted in §2.1.

^cFrom the mass ratio q and the application of Kepler’s Third Law.

^dComputed from the relative radii r_P and r_S and the orbital semimajor axis a .

^eComputed from $g = GM/R^2$

^fDirect result of the spectrophotometry analysis and photometrically-determined temperature ratio.

^gComputed from $L = 4\pi R^2 \sigma T_{\text{eff}}^4$

^hDirect result of the spectrophotometry analysis.

ⁱComputed assuming synchronous rotation.

^jComputed from $\log(L/L_{\odot})$ and $M_{\text{bol}\odot} = 4.75$

^kComputed from the synthetic V photometry, $E(B-V)$, and distance. Note that this result is consistent with expectations for mildly evolved early-B stars.

^lFrom the best-fitting isochrone to the data shown in Fig. 8.

^mUsing $(R_S/d)^2$ from the spectrophotometry analysis and R_S from the light curve and radial velocity curve analyses. See §6.

TABLE 6
DISTANCES TO LMC EB SYSTEMS

EB System	Reference	d_{EB}	d_{LMC} (Case I) ^a	d_{LMC} (Case II) ^b
HV 2274	Paper I,II	47.0 ± 2.2 kpc	45.9 kpc	47.0 kpc
HV 982	Paper II	50.2 ± 1.2 kpc	50.6 kpc	50.7 kpc
EROS 1044	This Paper	47.5 ± 1.8 kpc	47.3 kpc	47.4 kpc

^aDistance to a reference point at $(\alpha, \delta)_{1950} = (5^{\text{h}}24^{\text{m}}, -69^{\circ}47')$, corresponding to the optical center of the LMC's Bar according to Isserstedt 1975. Adopted LMC orientation defined by an inclination angle of 38° and a line-of-nodes position angle of 168° , from Schmidt-Kaler & Goehermann 1992.

^bDistance referred to the same reference point as above. Adopted LMC orientation defined by an inclination angle of 34.7° and a line-of-nodes position angle of 122.5° , from van der Marel & Cioni 2001.

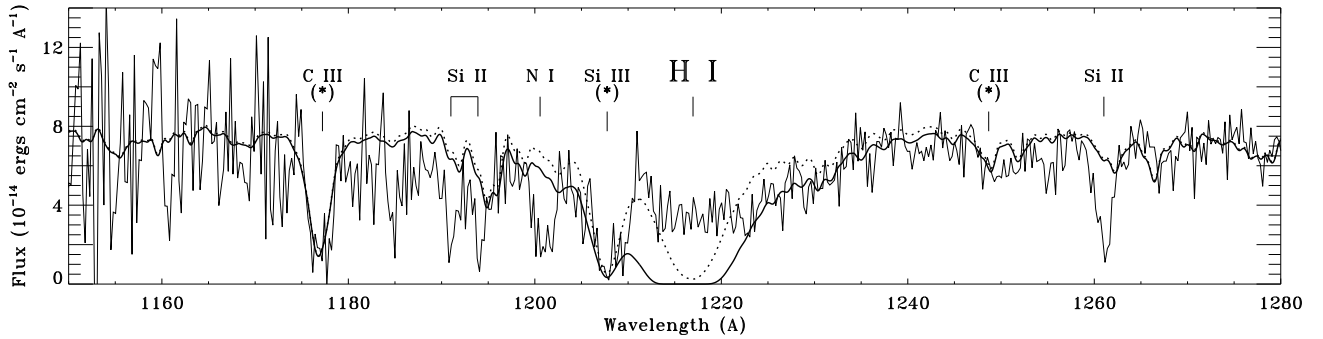


FIG. 6.— Derivation of the interstellar H I column density towards EROS 1044. The FOS data centered on the H I Ly α line at 1215.7 Å are shown (thin solid line). Prominent stellar features (denoted with an asterisk) and interstellar features are labeled. The dotted line represents a synthetic spectrum of the EROS 1044 system, constructed by combining two individual velocity-shifted spectra. (The “3rd light” contribution is negligible in this region.) The individual spectra were computed using Ivan Hubeny’s *SYSNPEC* spectral synthesis program with Kurucz *ATLAS9* atmosphere models of the appropriate stellar parameters as inputs. The solid curve shows the synthetic spectrum convolved with an interstellar H I Ly α line computed with a Galactic foreground component of $N(\text{H I}) = 5.5 \times 10^{20} \text{ cm}^{-2}$ at 0 km s $^{-1}$ and a LMC component of $N(\text{H I}) = 2.0 \times 10^{20} \text{ cm}^{-2}$ at 257 km s $^{-1}$ (see text in §4).

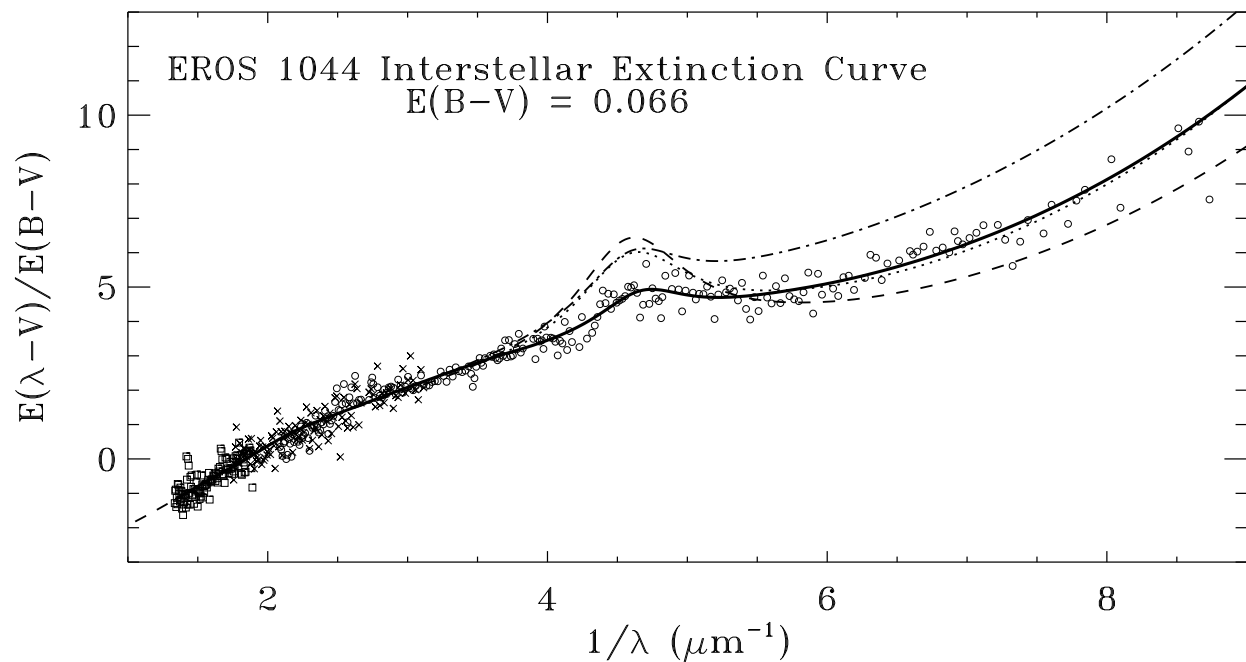


FIG. 7.— Normalized UV-through-optical interstellar extinction curve for EROS 1044. The thick solid line shows the parameterized form of the extinction curve as determined by the SED fitting procedure. The recipe for constructing such a “custom” extinction curve is taken from F99 and the parameters defining it are listed in Table 4. Small symbols indicate the actual normalized ratio of model fluxes to observed fluxes: circles, crosses, and squares indicate FOS, STIS G430L, and STIS G750L data, respectively. Shown for comparison are the mean Milky Way extinction curve for $R = 3.1$ from F99 (dashed line) and the mean LMC and 30 Doradus curves from Fitzpatrick (1986; dotted and dash-dotted lines, respectively). The EROS 1044 curve arises from dust in both the Milky Way ($E(B-V)_{\text{MW}} \simeq 0.055$) and the LMC ($E(B-V)_{\text{LMC}} \simeq 0.011$). The main attributes of the curve, its high far-UV level and extremely weak 2175 Å bump, are likely shared characteristics of the extinction in both environments.

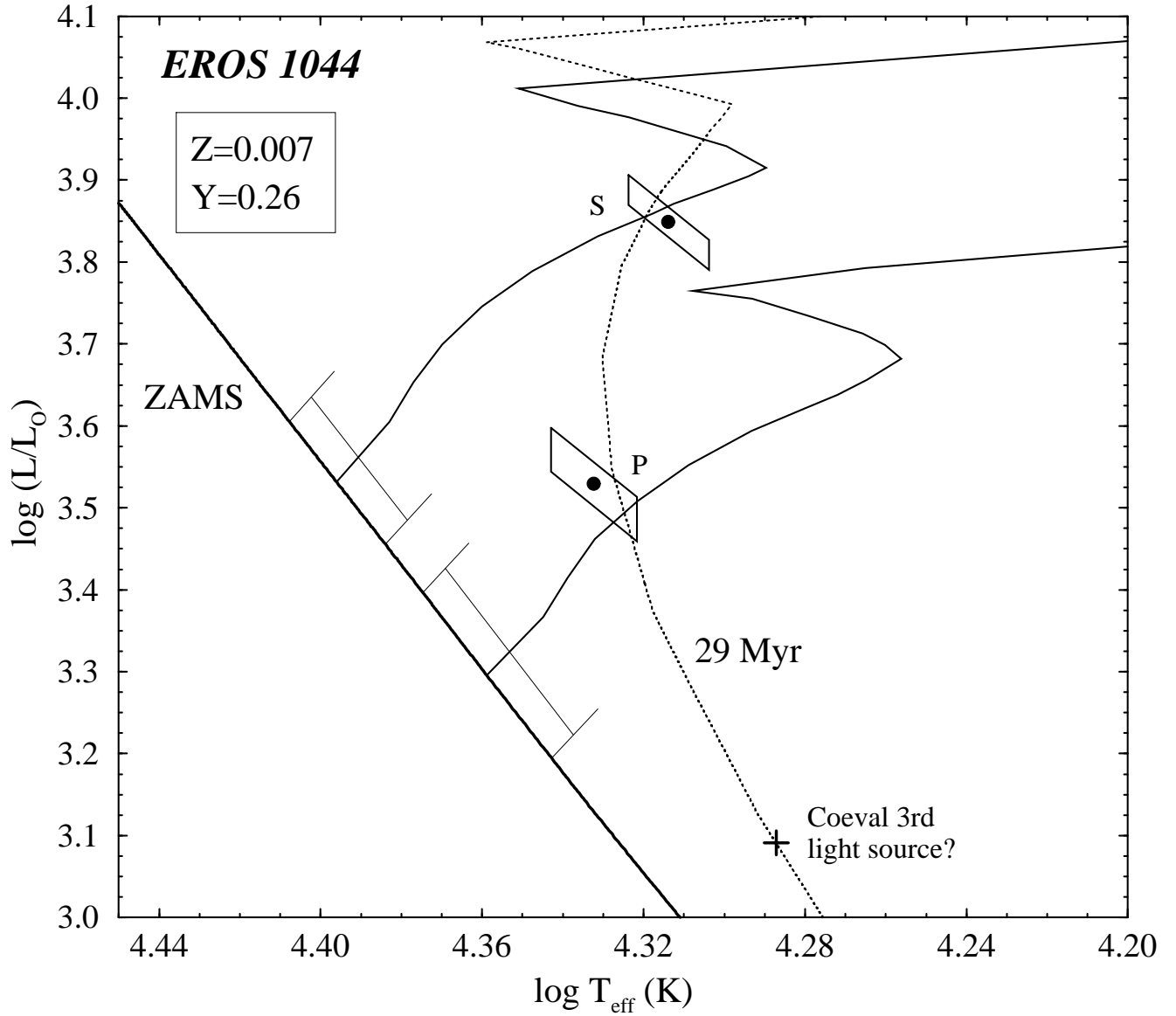


FIG. 8.— A comparison of the EROS 1044 results with stellar evolution theory. The positions of the the primary (P) and secondary (S) components on the $\log L$ vs. $\log T_{\text{eff}}$ diagram are indicated by the filled circles, with the skewed rectangles representing the 1σ error boxes. The two stellar evolution tracks shown (solid curves) correspond to the masses derived from the binary analysis. Error bars on the tracks near the ZAMS show the effect of 1σ uncertainties in the masses. The dotted line shows an isochrone corresponding to an age of 29 million years. The source and properties of the evolution tracks are discussed in §5. The plus sign indicates the position the “3rd light” component would occupy if it were coeval with the EB system.